The Impact of Transition and Turbulence Modeling on the SPLEEN High-Speed Low-Pressure Turbine Cascade

ASME Journal of Turbomachinery
Online journal at:
https://asmedigitalcollection.asme.org/turbomachinery

Leonardo Metti
Department of Industrial Engineering,
University of Florence,
Via Santa Marta 3,
50139 Florence, Italy
e-mail: leonardo.metti@unifi.it

Michele Marconcini[1]
Department of Industrial Engineering,
University of Florence,
Via Santa Marta 3,
50139 Florence, Italy
e-mail: michele.marconcini@unifi.it

Simone Salvadori
Department of Energy,
Politecnico di Torino,
Corso Duca degli Abruzzi 24,
10124 Torino, Italy
e-mail: simone.salvadori@polito.it

Daniela Anna Misul
Department of Energy,
Politecnico di Torino,
Corso Duca degli Abruzzi 24,
10124 Torino, Italy
e-mail: daniela.misul@polito.it

Nicola Rosafio
Department of Energy,
Politecnico di Torino,
Corso Duca degli Abruzzi 24,
10124 Torino, Italy
e-mail: nicola.rosafio@polito.it

Gustavo Lopes
Department of Turbomachinery and Propulsion,
von Karman Institute for Fluid Dynamics,
Waterloosesteenweg 72,
1640 Sint-Genesius-Rode, Belgium
e-mail: gustavo.lopes@vki.ac.be

Sergio Lavagnoli
Department of Turbomachinery and Propulsion,
von Karman Institute for Fluid Dynamics,
Waterloosesteenweg 72,
1640 Sint-Genesius-Rode, Belgium
e-mail: sergio.lavagnoli@vki.ac.be

The Impact of Transition and Turbulence Modeling on the SPLEEN High-Speed Low-Pressure Turbine Cascade

In high-speed low-pressure turbines (LPTs) for geared turbofan engine applications, transonic flow conditions combined with low Reynolds number operation depict a flow scenario where shock waves can interact with laminar or turbulent boundary layers, and the resulting flow topologies pose serious challenges for computational fluid dynamics (CFD) analyses. In this work, two different in-house developed Reynolds-averaged Navier–Stokes (RANS) solvers are applied to the study of a transonic low-pressure turbine cascade over a range of Mach and Reynolds numbers, with a focus on the performance of transition/turbulent closures. The selected test case consists of the SPLEEN (Secondary and Leakage Flow Effects in High-Speed Low-Pressure Turbines) C1 cascade, a state-of-the-art high-speed low-pressure turbine blade section that has been investigated in an extensive experimental campaign at the von Kármán Institute, in the framework of the SPLEEN European Research Programme. The considered transition-sensitive turbulence closures are representative of the most advanced techniques for RANS methods and range from correlation-based intermittency transport approaches to phenomenological model based on the laminar kinetic energy (LKE) concept and the $k - v'^2 - \omega$ framework. It is shown how realistic transition modeling is crucial for predicting blade loading distributions and then addresses design challenges for transonic LPT bladings. A discussion concerning the reproduction of wake loss profiles demonstrates how classical linear eddy viscosity closures can be adequate in the case of attached flow even in transonic flow conditions but fall short in predicting the intense wake mixing brought about by the thick turbulent boundary layers that are formed past laminar separation bubbles. [DOI: 10.1115/1.4069487]

Keywords: high-speed low-pressure turbine, SPLEEN, computational fluid dynamics, transition modeling, boundary layer separation

[1]Corresponding author.
Contributed by the International Gas Turbine Institute (IGTI) of ASME for publication in the JOURNAL OF TURBOMACHINERY. Manuscript received June 5, 2025; final manuscript received July 22, 2025; published online September 19, 2025. Tech. Editor: David G. Bogard.

Yuan Fang
Department of Mechanical Engineering,
University of Melbourne,
Melbourne, VIC 3010, Australia
e-mail: fang.y5@unimelb.edu.au

Richard D. Sandberg
Department of Mechanical Engineering,
University of Melbourne,
Melbourne, VIC 3010, Australia
e-mail: richard.sandberg@unimelb.edu.au

Roberto Pacciani
Department of Industrial Engineering,
University of Florence,
Via Santa Marta 3,
50139 Florence, Italy
e-mail: roberto.pacciani@unifi.it

1 Introduction

A reduction in specific fuel consumption has a direct impact on the carbon footprint of an aircraft engine. In recent years, there has been a notable shift toward the adoption of geared ultra-high bypass ratio turbofan engine configurations [1]. In particular, decoupling the rotational speeds of the low-pressure turbine (LPT) and fan via a gearbox allows for a reduction in the number of stages of the LPT. This configuration permits the LPT rotors to rotate at high speeds, resulting in transonic flow at the blade trailing edge. Conversely, the operating Reynolds number of the LPT exhibits considerable variation between take-off and cruise configurations, decreasing from approximately 5×10^5 to 0.5×10^5 [2]. This indicates that a predominantly turbulent boundary layer is present at take-off, while extensive laminar regions, prone to transition, are present at cruise. Consequently, new-generation geared LPTs present a configuration in which compressibility phenomena interact with transitional boundary layers, the prediction of which is fundamental to evaluate the design performances [3].

The boundary layer transition can occur in three main modes: natural, bypass, and separated flow [4]. Natural transition is characterized by the linear amplification of perturbations within the laminar boundary layer, which subsequently evolve into three-dimensional instabilities, resulting in the formation of turbulent spots [5]. When the freestream turbulence level exceeds 1%, the transition from laminar to turbulent generally occurs, bypassing some of the pretransitional features. This mode is referred to as the bypass transition. Additionally, the transition may be triggered by the separation of the laminar boundary layer, which can then result in turbulent reattachment or the formation of an open bubble. In LPTs, bypass and separated-flow transition are the most common transition modes. Usually, the dominant mechanism cannot be determined a priori, and sometimes different modalities may interact, thus generating a mixed character of the transition physics [5].

In recent years, there have been significant developments in high-performance computing resources, which have enabled the feasibility of high-fidelity calculations such as large eddy simulation and direct numerical simulation [6–8]. Nevertheless, their high computational cost makes them unsuitable for use in an iterative industrial design process [9]. Consequently, in the current context, (U)RANS calculations remain the primary tool relied upon in an industrial design chain.

In the field of computational fluid dynamics (CFD), boundary layer transition modeling is divided into two families of methods. An overview of the main approaches and methods used in the field of turbomachinery is summarized in Ref. [10]. The first family is correlation based. One of the prominent examples is a concept known as intermittency, which defines a fully laminar state as zero, a fully turbulent state as one, and the range between zero to one as the transitional state. Among the transition models based on intermittency, the most widely used is the $\gamma - \mathrm{Re}_\theta$ model proposed by Menter [11]. Numerous other algebraic or transport models can be found in the literature [11–13]. A variant of the $\gamma - \mathrm{Re}_\theta$ is the γ model introduced in Ref. [14], which is based on intermittency transport only. The second family of models is physics-based. A typical example is based on the concept of laminar kinetic energy (LKE), originally proposed by Mayle and Schultz [15], describing the pretransitional fluctuations. There are also many examples in the literature where a model based on LKE has been successfully implemented and applied in turbomachinery [16–19]. In the latter case, in particular, the LKE model has been reformulated to enable multimodal transition prediction, with a focus on the possibility of data-driven improvement by means of machine-learning strategies. In addition to LKE, other physics-based transition parameters have been proposed, such as v'^2, which represents the pretransitional, wall-normal velocity fluctuations in the laminar boundary layer and the three-dimensional turbulent fluctuations in the turbulent boundary layer. Lopez and Walters [20] constructed the $k - v'^2 - \omega$ model, where the transitional parameter varies depending on the boundary layer state. However, there are currently only a limited number of studies in the literature where this model has been applied to turbomachinery environments [21,22].

The flow topology in high-speed LPTs is characterized by complex interaction phenomena between transonic flows and transitional boundary layers, creating a quite unique and highly challenging scenario for Reynolds-averaged Navier–Stokes approaches. This article presents a comprehensive CFD study of the SPLEEN (Secondary and Leakage Flow Effects in High-Speed Low-Pressure Turbines) C1 cascade, with the aim of seeking a numerical setup amenable for guiding the design of the next generation of LPTs for geared turbofan engines. The cascade has been experimentally investigated at the von Kármán Institute for Fluid Dynamics as the major part of the European Research Programme SPLEEN [23–25]. Such a research project was intended to provide benchmarks for state-of-the-art high-speed LPTs. One interesting aspect of the SPLEEN test case is the topology of the boundary layer on the suction side. At subsonic exit Mach number flow configurations, the suction side boundary layer transition occurs due to the presence of a separation bubble. When increasing the Reynolds number, the transition onset moves toward the trailing edge as the separation bubble size is reduced. As Mach number increases, the transition becomes bypass/shock-induced, thus acquiring a multimodal character. High-fidelity calculations of such a test case are available in the literature [26–28], but there are fewer examples of (U)RANS calculations applied to the SPLEEN cascade [22]. In this work, two different state-of-the-art (U)RANS solvers, equipped with several modern transition-sensitive turbulence closures, are

applied to study the SPLEEN C1 test case across a range of Reynolds and Mach numbers. The purpose of the study is to assess the performance of the selected transition/turbulence models, highlighting their strengths and limitations in capturing blade loading distribution and losses, and scrutinizing their abilities to reproduce the transition path and wake mixing.

The article is structured as follows: Sec. 2 provides a brief introduction about the SPLEEN project. With a focus on transition modeling, the computational framework of two different flow solvers used for the calculation will be presented in Sec. 3. Section 4 deals with the setup of the calculation, in terms of turbulent boundary conditions and grid independency. Results will be shown and commented in Sec. 5. Specifically, the particle image velocimetry (PIV) data will be compared with CFD results to evaluate the accuracy of the numerical flow configuration. Subsequently, distributions of relevant key quantities will be analyzed. The transition models will be assessed in terms of blade distributions of isentropic Mach number and wall shear stresses, providing insights on the underlying physical phenomena. Finally, the wake pressure loss and turbulent kinetic energy downstream of the blade will be examined and discussed.

2 SPLEEN Test Case

The test case investigated in this work is the SPLEEN C1, an open-access database of experimental data collected at the von Kármán Institute for Fluid Dynamics within the H2020 Clean Sky 2 SPLEEN project. Detailed description of the test case can be found in Refs. [23,24]. The linear cascade is representative of a rotor airfoil in a modern configuration of high-speed LPT. Measurements are conducted in the high-speed, low Reynolds facility S-1/C at the von Kármán Institute. The wind tunnel is a continuous closed-loop facility driven by a 13-stage axial flow compressor, whose rotational speed adjustment together with a pressure regulation valve allows the imposition of the mass flow. The cascade test section is located in the first elbow of the wind tunnel following the diffuser.

The SPLEEN test case includes wake generators upstream of the cascade and cavity flows. In the present work, only a steady inlet with no purge flow has been considered. The test section is depicted in Fig. 1(*a*). The freestream turbulence was imposed with an upstream passive grid, composed of a mesh size of 12 mm and rods with a diameter of 3 mm. The detailed characterization of turbulent quantities is described in Sec. 4.1. The geometrical data of the SPLEEN C1 cascade is summarized in Table 1.

Figure 1(*b*) shows reference planes used for measurements. Planes 01 and 02 are located upstream of the cascade, $1.12C_{ax}$ and $0.5C_{ax}$ distant from the leading edge, respectively, while Planes 05 and 06 are downstream of the blade, $0.25C_{ax}$ and $0.50C_{ax}$ from the trailing edge, respectively. Total pressure and total temperatures are measured upstream of the grid with an absolute pressure sensor (WIKA P-30) and a bare K-type thermocouple, respectively. Total pressure at Plane 01 is then found using a correlation [23].

The test case is heavily instrumented; here, only the sensors used to acquire the measurements for the CFD comparison are reported. On Plane 02, a hot cross-wire probe (XW01) is used for inlet turbulence measurement, while on Plane 06, total pressure loss is obtained from a set of miniature pneumatic 5-hole L-shaped probes. The blade distributions of isentropic Mach number are computed using pressure tap measurements, and surface mounted hot films are used to compute the qualitative distribution of wall shear stress. A detailed description of all the instrumentation can be found in Ref. [23].

Regarding PIV measurements, Fig. 2 illustrates the field of view for the blade-to-blade (B2B) PIV configurations carried out for the SPLEEN C1 cascade. The first configuration aims measurements on the mid-span B2B plane at the cascade inlet plane using a stereoscopic two-dimensional three-component PIV setup. The second configuration measures at the mid-span B2B plane within the cascade passage, including a part of the cascade outlet, using a planar two-dimensional two-component PIV setup with a side-by-side camera arrangement. In this work, only the second configuration was considered for CFD comparison. The data related to turbulence on Plane 06 are used to compare turbulent kinetic energy (TKE) profiles between the experimental results and CFD calculations. Further details of the PIV test campaign can be found in Ref. [25].

3 Computational Framework

3.1 HybFlow Solver. HybFlow is a cell-centered finite volume solver originally developed at the University of Florence [29–31] and currently under development at the Politecnico di Torino [22,32]. The code solves the conservative form of Navier–Stokes equations on hybrid grid topologies. The inviscid fluxes are computed using Roe's scheme [33], while viscous fluxes are approximated by means of cell gradients plus a penalization term according to Ref. [34]. Variable reconstruction is performed by means of a least-square method [35], which achieves second-order accuracy on unstructured grid topologies. A steady solution is achieved by means of a pseudo-transient technique based on a damped Newton method with Krylov acceleration. At each numerical time step, the solution of the linear system is found by means of a preconditioned Generalized Minimum Residual (GMRES) solver

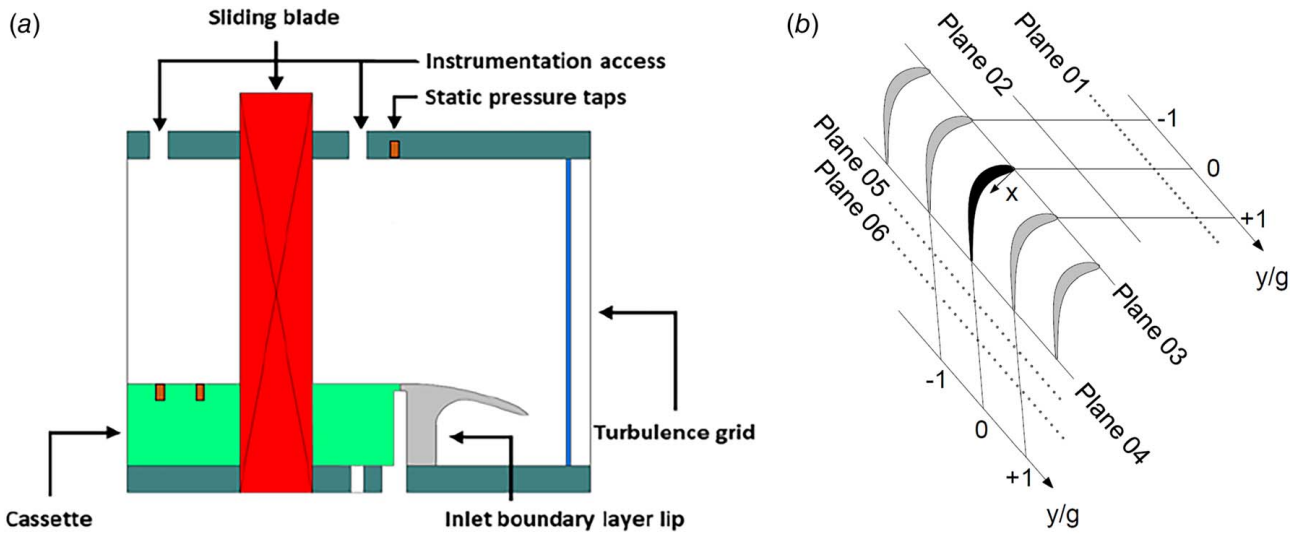

Fig. 1 SPLEEN C1 test section (*a*) and measurement planes (*b*)

Table 1 Geometry of the SPLEEN C1 cascade

Axial chord C_{ax}	47.61 mm
Stagger angle σ	24.4 deg
Pitch g	32.95 mm
Inlet metal angle α_{in}	37.3 deg
Outlet metal angle α_{out}	53.8 deg

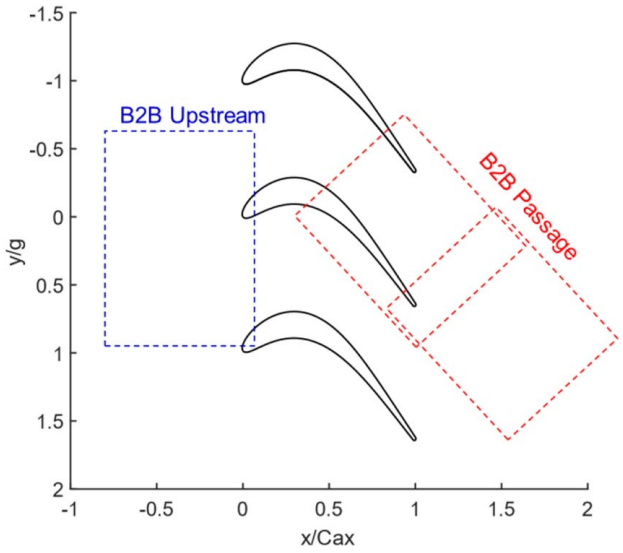

Fig. 2 Field of view of PIV blade-to-blade measurements

[36]. The preconditioner is based on a serial 1-level additive Schwarz method, obtained with the Incomplete Lower-Upper (ILU)) factorization of local matrices [37].

The transition-sensitive k-ν'^2-ω model by Ref. [20] is used for numerical calculations. In this model, the transition is controlled by means of a term that can be directly linked to pressure-strain terms, providing a more general framework for physics-based transition modeling. The model activates the transition using two terms, allowing it to account for both bypass and natural transitions. A detailed description of the model characteristics and its implementation in the HybFlow solver is available in the works by Refs. [22,32].

The mesh independence test for the HybFlow solver was assessed using four different grids, with the total number of elements ranging from 50×10^3 to 100×10^3 [22]. The analysis was performed for the nominal conditions of the cascade ($Ma_{out,is} = 0.9$, $Re_{out,is} = 70,000$). The main characteristics of the meshes, along with a detailed analysis of the grid dependence in terms of blade loading and wake characteristics, were summarized in the work by Ref. [22]. It is worth mentioning here that the blade loadings obtained with all the investigated meshes converged to the same result. However, the variability of the results obtained for the wake shape analysis allowed us to select a computational grid consisting of $\approx 90 \times 10^3$ total elements, with 25 quadrilateral layers and a maximum y^+ of 0.12.

3.2 TRAF Solver. TRAF is a state-of-the-art density-based solver developed in-house at the University of Florence that has been extensively validated in turbomachinery configurations, particularly for cascade flows, across a range of conditions from incompressible to supersonic flows [38–40]. It is a steady/unsteady, multigrid/multiblock solver for the Reynolds-averaged Navier–Stokes equations on structured grids. In terms of numerical fluxes, the scheme that has been considered in the present work relies on a formally third-order total variation diminishing MUSCL (Monotonic Upstream-centered Scheme for Conservation Laws) framework, based on the generalized min-mod limiter [39], built on top of the Roe upwind scheme.

Several transition and turbulence models are available in TRAF. For the present work, the following transition models have been considered: the Langtry and Menter $\gamma - Re_{\theta,t}$ model [11], the Menter's γ model [14], and a newly developed LKE-based framework [19]. In this latter approach, the LKE transport equation has been reformulated to address the growth of pretransitional fluctuations in attached and separated shear layers under the effects of pressure gradient and freestream turbulence, so that it is suitable for modeling both bypass and separated-flow transition. A detailed and complete description of the model formulation can be found in Pacciani et al. [19]. For all the considered transition models, the coupled turbulence closure is the $k - \omega$ SST turbulence model [19].

4 Setup

The CFD numerical domain is illustrated in Fig. 3. The inlet plane is coincident with Plane 01, while the outlet is located after Plane 06, at a distance equal to 30% of the axial chord. The mesh consists of an O-type block surrounding the blade, with two H-type blocks positioned upstream and downstream of the profile, respectively. The fluid is assumed to be a perfect gas with $\gamma = 1.4$ and $R = 287.07\,\mathrm{J/(kg\,K)}$. The flow conditions are set imposing $Re_{out,is}$ and $Ma_{out,is}$, which are defined as

$$Re_{out,is} = \frac{\rho_{out,is} CV_{out,is}}{\mu_{out,is}} \tag{1}$$

$$Ma_{out,is} = \sqrt{\frac{2}{\gamma - 1}\left[\left(\frac{p_{out}}{p_{0,in}}\right)^{-\frac{\gamma-1}{\gamma}} - 1\right]} \tag{2}$$

The inlet total pressure $p_{0,in}$ and the outlet static pressure p_{out} are determined to obtain a pressure ratio that matches the desired $Ma_{out,is}$ and $Re_{out,is}$ for a fixed total temperature of $T_{0,in} = 300\,K$. Operating conditions cover the range $Ma_{out,is} = 0.70 \div 0.95$ and $Re_{out,is} = 65k \div 120k$. Finally, an inflow angle of $\beta = 36.69$ deg is imposed. Turbulence boundary conditions provided at the inlet are turbulence intensity Tu and turbulent length scale L_t. The setting of these latter parameters along with the analysis of turbulent decay will be addressed in Sec. 4.1.

Steady analysis will be carried out considering a bi-dimensional mid-span section. The chosen turbulence models are $k - \omega$ SST, while the selected transition models are LKE, γ or $\gamma - Re_{\theta,t}$ models.

4.1 Turbulence Decay. The values of Tu_{in} and $L_{t,in}$ must be determined to match the experimental turbulent decay, which is measured at Plane 02 by XW. The turbulent generating grid is mounted orthogonal to the inlet flow direction, and then inclined relative to the cascade pitch-wise direction. The decay law for the turbulent intensity was then measured by traversing in the pitch-wise direction. To facilitate the comparison with the calculated decay law, the experimental Tu pitch-wise distribution has been projected onto the inlet flow direction, as shown in Fig. 4(*a*). The turbulence intensity Tu is defined as

$$Tu = \frac{\sqrt{\frac{1}{3}(u'^2 + v'^2 + w'^2)}}{V} \tag{3}$$

The cross-wire probe allows the estimation of only two components of velocity in the blade-to-blade plane, so the third component w'^2 is assumed to be equal to the mean of u'^2 and v'^2. The planar turbulence intensity, hence with $w'^2 = \frac{1}{2}(u'^2 + v'^2)$, and the isotropic

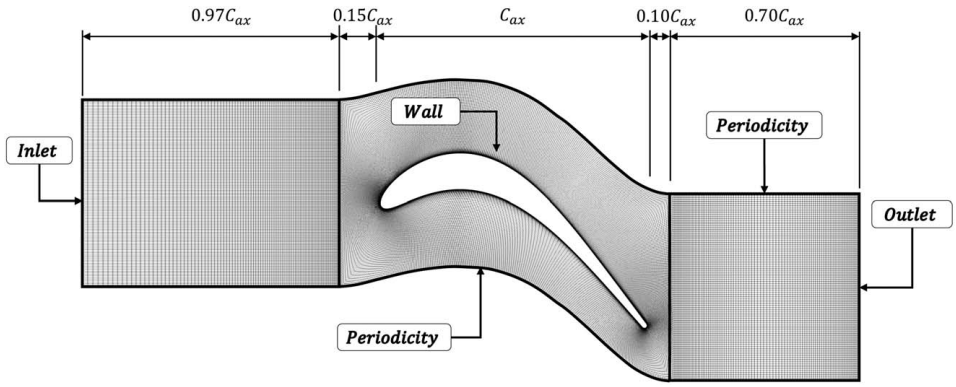

Fig. 3 Numerical domain with boundary type specification

turbulence ($u'^2 = v'^2 = w'^2$) can then be defined as

$$\mathrm{Tu}_{2D} = \frac{\sqrt{\frac{1}{2}(u'^2 + v'^2)}}{V} \tag{4}$$

$$\mathrm{Tu}_{iso} = \frac{\sqrt{u'^2}}{V} \tag{5}$$

The turbulent decay matching is performed on the design configuration ($\mathrm{Ma}_{out,is} = 0.90$, $\mathrm{Re}_{out,is} = 70\,\mathrm{k}$), as this is the only case for which cross-wire measurements are available. The assumption is also made that the turbulent boundary conditions derived from the decay matching of the latter case are valid for the other flow configurations. The modeling of turbulence in CFD calculations follows the assumption of isotropic turbulence, so Tu is defined as $\sqrt{2/3\,k}/V$. The results of the decay matching are shown in Fig. 4(*b*). The experimental database provides the decay in terms of Tu_{2D} and Tu_{iso}, and the turbulent boundary conditions differ depending on whether one chooses to match one or the other. Specifically, the decay matching yields the turbulent boundary conditions summarized in Table 2.

The increase in turbulence level recorded near the blade leading edge is the result of relevant nonuniformities in the velocity field due to the potential effect induced by the blades. Such a behavior is consistently observed in RANS calculations with linear eddy viscosity models. The increase in Tu, as the cascade is approached, changes in magnitude in the pitch-wise direction, but it can hardly be eliminated.

To investigate the effects of the different turbulent boundary conditions, the shift of transition onset on the suction side for the configuration with $\mathrm{Ma}_{out,is} = 0.70$, $\mathrm{Re}_{out,is} = 100\mathrm{k}$ between the different transition models is analyzed (Fig. 5). Comparisons are carried out first using the values from matching the isotropic data, followed by those from matching the 2D data. It is observed that with isotropic boundary conditions, the turbulence level at the leading edge of the blade is higher, causing the transition to occur earlier. However, when 2D conditions are imposed, resulting in lower Tu at the leading edge, the shift of the transition point is minimal and practically negligible for all the considered transition/turbulence models. Therefore, matching isotropic or 2D turbulent decay data is effectively equivalent. For the present calculations, the isotropic matching has been used.

4.2 Mesh Sensitivity. As previously stated, for TRAF calculations, a structured mesh comprising three blocks is employed. The O-type grid ensures optimal mesh quality in the boundary layer and blade passage, while the H-type blocks guarantee the highest degree of grid uniformity and orthogonality, thereby ensuring the most accurate capture of turbulent decay and wakes. To analyze the grid dependency of the calculations, five different meshes have been generated, designated M1 to M5 in ascending order of refinement. As can be observed in Table 3, in addition to the number of cells in each block, the height of the first wall element is also varied. In Table 3, mesh skewness has been estimated in Paraview by using the standard mesh quality tool [41]. It is noteworthy that, as the boundary layer is predominantly laminar on the blade, it is more convenient to characterize the wall spacing by the height of the first cell rather than by parameters such as y^+.

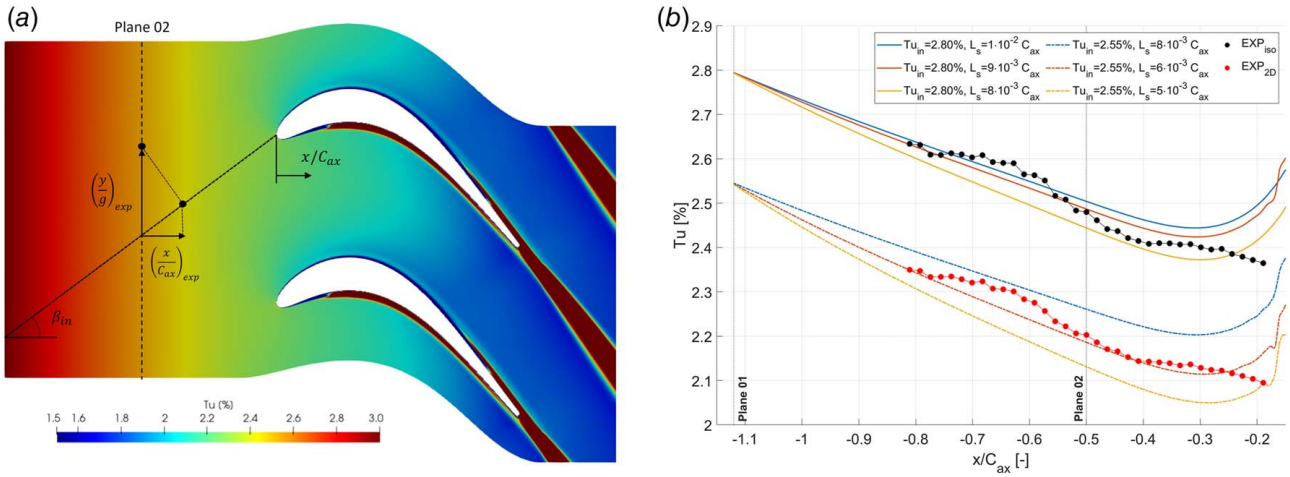

Fig. 4 Turbulence decay: contour and stream-wise projection (*a*) and experimental matching with 2D and isotropic data (*b*)

Table 2 Turbulence intensity and turbulent length scale at inlet, based on matching with 2D isotropic experimental data

	ISO	2D
Tu_{in}	2.80%	2.55%
$L_{t,in}$	0.428 mm (0.9%C_{ax})	0.286 mm (0.6%C_{ax})

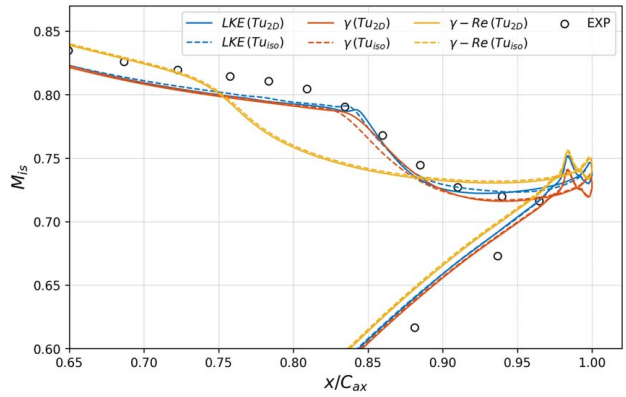

Fig. 5 Isentropic Mach on blade with different models using 2D and isotropic turbulent decay matching ($Ma_{out,is} = 0.70$, $Re_{out,is} = 100$ k)

Table 3 Mesh parameters in terms of number of cells, dimensionless first cell height h_{wall}, y^+, maximum skewness, minimum, and maximum cell area scaled with C_{ax}^2

	Cells	h_{wall}	y^+_{max}	$skew_{max}$	A_{min}	A_{max}
M1	30,160	2.5×10^{-4}	1.08	0.79	4.9×10^{-7}	3.6×10^{-4}
M2	48,960	1.0×10^{-4}	0.42	0.80	1.0×10^{-7}	1.9×10^{-4}
M3	76,560	7.5×10^{-5}	0.32	0.81	7.5×10^{-8}	1.2×10^{-4}
M4	103,696	6.5×10^{-5}	0.27	0.86	6.3×10^{-8}	9.8×10^{-5}
M5	123,520	5.5×10^{-5}	0.21	0.88	4.4×10^{-8}	8.1×10^{-5}

Grid dependence analysis is performed on the design case $Ma_{out,is} = 0.90$, $Re_{out,is} = 70$k. Figure 6(*a*) illustrates that blade loading remains approximately constant using different grids. The isentropic Mach distribution on the suction side is essentially unaltered, whereas the pressure side exhibits the most notable discrepancies. The convergence of the calculation is adversely affected by the presence of a bubble in this section. Consequently, the two coarsest grids (M1, M2) are unable to stabilize in terms of M_{is}.

With regard to the total pressure loss in the wake of Plane 06, it can be observed that as the grid coarseness increases, there is a corresponding decrease in agreement with the experimental data. In particular, a coarse grid exhibits a larger numerical diffusion, which results in a reduction in the total pressure peak and an increase in the thickness of the wake. The best results are obtained for M4 and M5 grids, which provide similar results.

Therefore, it is determined that the most suitable trade-off in terms of accuracy and computational cost can be achieved with the M4 grid. For these reasons, the analyses will henceforth be conducted using the M4 grid.

5 Results and Discussion

This section presents a comparative analysis of the results obtained from the various transition models, aiming to identify the distinctive characteristics of each. The analysis begins with an examination of the flow field in the different configurations, which will be compared with the PIV data. This is followed by a more comprehensive quantitative analysis, with a particular focus on the boundary layer transition. Finally, the study compares the wake losses at Plane 06, examining pitch-wise distributions of total pressure and turbulence intensity.

5.1 Flow Field Analysis. PIV measurements provide Mach contours and turbulence intensities within the blade passage and downstream of the row. To compare PIV and CFD flow fields, the error for a given quantity ϕ is defined as

$$\text{Error} = \frac{\phi_{CFD} - \phi_{PIV}}{\phi_{PIV}} \tag{6}$$

By this definition, a positive value of the error means that the CFD overestimates the PIV data, and vice versa with a negative error. The comparison is only exhibited within the passage. Close to solid walls PIV suffers from low seeding, hence compromising the cross-correlation process for determining velocity field. In this work, a filter has been applied to PIV data to exclude from the domain low seeding areas.

For comparison with PIV, the results from the TRAF LKE transition model have been used. In general, however, the flow field predicted by the different models show only slight differences, with the variations primarily observed at the blade surface and in the total pressure loss within the wakes.

Figure 7 shows the Mach distributions of the subsonic configurations ($Ma_{out,is} = 0.70$) with $Re_{out,is} = 120$k. The agreement between PIV and CFD within the passage is high, with an error of less than 5%. Both effectively capture the flow acceleration on the suction side, with a maximum Mach number reaching approximately 0.80.

Figures 8 and 9 depict transonic configurations with $Ma_{out,is} = 0.90$ and $Ma_{out,is} = 0.95$, respectively, and a $Re_{out,is} = 70$k. In these cases, the presence of a passage shock is evident in the blade throat region. The upstream Mach number is approximately 1.04 for $Ma_{out,is} = 0.90$ and 1.10 for $Ma_{out,is} = 0.95$. The position of the shock is accurately reproduced, except in the case $Ma_{out,is} = 0.95$, where the error is slightly larger but still within an acceptable range, remaining below 10%.

A comparison between PIV and CFD in the case of $Ma_{out,is} = 0.70$ and $Re_{out,is} = 120$k in terms of turbulence intensity is presented in Fig. 10. The background turbulence within the blade passage predicted by CFD is around 1.0%, against the one measured by PIV of 1.6%, with an error of approximately 40%. Furthermore, the wake is also not accurately captured, with the first section near the trailing edge exhibiting an error of up to 50%, which then decreases away from the profile. In general, the results in terms of turbulence intensity are not particularly satisfactory, and the same conclusions can be drawn from other flow configurations. Accurate assessment of turbulence intensity in the wakes will be performed by analyzing pitch-wise distributions in Plane 06.

5.2 Isentropic Mach Number Distributions. As already mentioned in the introduction section, the SPLEEN test case features a separating boundary layer on the suction side, resulting in separation bubbles characterized by sizes and positions that are highly dependent on the operating conditions. The suction side boundary layer topology is also affected by the interaction with the shock system that forms at high $Ma_{out,is}$.

Figure 11 illustrates the isentropic Mach distributions on the blade. For the sake of conciseness, only the results for two Reynolds numbers ($Re_{out,is} = 70$k, 120k) and three Mach numbers ($Ma_{out,is} = 0.7, 0.8, 0.9$) are reported. Before analyzing in detail, the complex suction side boundary layer scenario, it is worthwhile to discuss the pressure side flow features. The first 40% of the blade chord is of particular interest as nonnegligible differences among the various predictions and the experimental data are

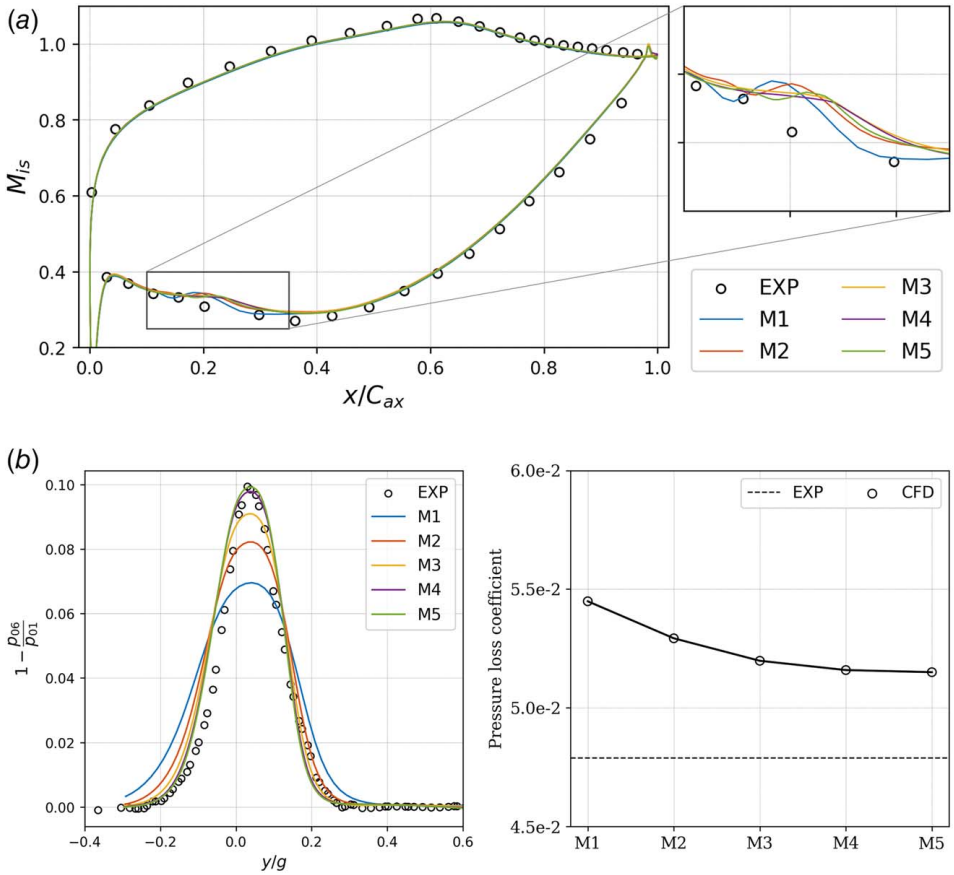

Fig. 6 Isentropic Mach on blade (*a*) and total pressure loss at Plane 06 (*b*) for different grids with $Ma_{out,is} = 0.90$, $Re_{out,is} = 70$ k

seen to occur in such a region. All the calculations report the presence of a separation bubble. Its size and configuration are different depending on the particular transition/turbulence closure considered; nevertheless, it is able to impact the computed M_{is} distribution in a more or less subtle way. The discrepancies between predictions and measurements suggest that the PS separation bubble could be consistently overestimated by all the calculations.

Among these, the $k - v^2 - \omega$ model displays the highest inaccuracy, suggesting the reproduction of a too large separation bubble. It is not possible to discern, from the measured M_{is} distributions, whether a separation bubble is actually present in the experimental flow configurations or not. The discussion on this issue is then moved to the next section of the article, where wall shear stress distributions will be analyzed.

For all the considered Reynolds numbers, the isentropic Mach number distributions suggest the presence of a suction side separation bubble from $Ma_{out,is} = 0.7$ up to $Ma_{out,is} = 0.8$. The separation bubble length decreases as the exit Mach number increases. In such flow configurations, transition occurs due to separated flow. The transition onset location, identified as the location in the separated flow region where pressure recovery starts, tends to move toward the trailing edge as the exit Reynolds and Mach numbers increase.

The captured bubble size has a nonnegligible influence on the of the M_{is} distribution on the entire suction side. The longer the predicted bubble length, the lower the suction side M_{is} peak and overall level. This trend is particularly evident for $Ma_{out,is} = 0.7$. For this exit Mach number, the $\gamma - Re_{\theta,t}$ model predicts too early transition and the smallest separation bubble relative to

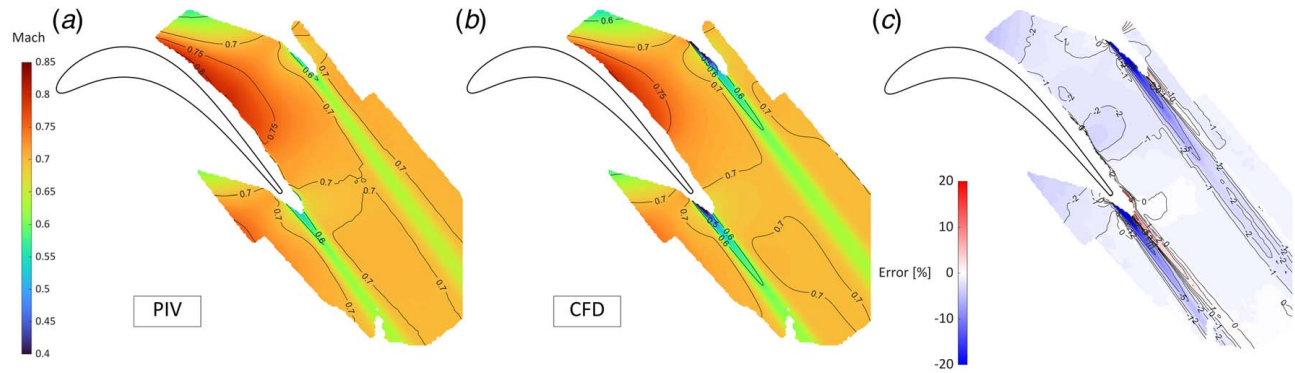

Fig. 7 Mach contours for $Ma_{out,is} = 0.70$, $Re_{out,is} = 120$ k with PIV (*a*), TRAF (*b*), and relative error (c)

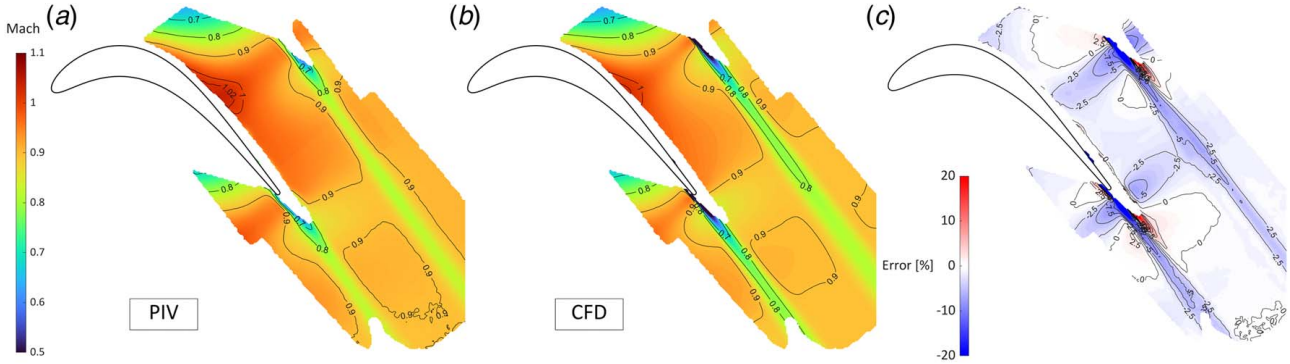

Fig. 8 Mach contours for $Ma_{out,is} = 0.90$, $Re_{out,is} = 70$ k with PIV (*a*), TRAF (*b*), and relative error (*c*)

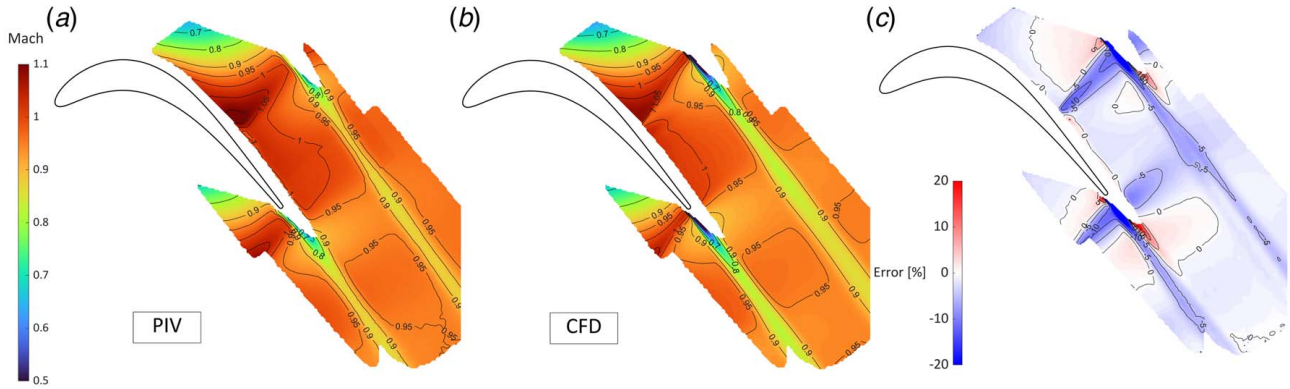

Fig. 9 Mach contours for $Ma_{out,is} = 0.95$, $Re_{out,is} = 70$ k with PIV (*a*), TRAF (*b*), and relative error (*c*)

measurements. As a consequence, it shows a slight M_{is} overestimation along the blade SS. All the calculations (but the $\gamma - Re_{\theta,t}$ ones) tend to underestimate the isentropic Mach number on the suction side even when the captured separation bubble structure is in agreement with the measured one (Fig. 11). The model that appears to most accurately represent the onset of the transition and consequently the separation bubble is the γ model, as can be observed in Fig. 11. The LKE model is also quite accurate in low Mach number cases. However, when the transition point is in close proximity to the trailing edge (as in the case of $Ma_{out,is} = 0.70$ and $Re_{out,is} = 70$k), it fails to trigger the transition. This behavior is analogous to that of $k - v'^2 - \omega$, the distinction being that the latter delays bubble reattachment in all the low Mach number cases, thus exhibiting perhaps the poorest performance among the models. The underestimation of the freestream turbulence level in the blade passage is evidenced in Fig. 10 may have an impact on the predicted transition onset and reattachment locations. However, the response to freestream turbulence and pressure gradient by the various models clearly depends on the Reynolds number and becomes more realistic as $Re_{out,is}$ is increased. A detail of the isentropic Mach distribution in the transition onset zone for the case with $Ma_{out,is} = 0.70$ is depicted in Fig. 12 for better visualization.

Coming to the high Mach number cases ($Ma_{out,is} = 0.9$, Fig. 11), all the calculations, except for the $\gamma - Re_{\theta,t}$, are in good agreement with the experimental data, even if a slight underestimation of the suction side M_{is} distribution can still be appreciated. The early transition predicted by the $\gamma - Re_{\theta,t}$ model results in a misrepresentation of the isentropic Mach number behavior in the last 20% of the axial chord along the blade suction side. This is particularly evident for the $Re_{out,is} = 120$k flow configuration, but it can also be appreciated for $Re_{out,is} = 70$k.

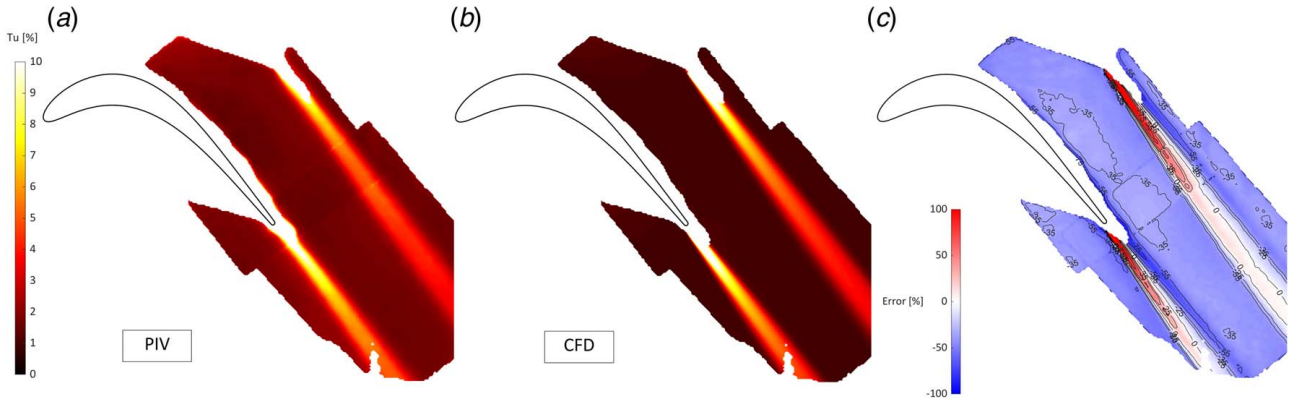

Fig. 10 Tu contours for $Ma_{out,is} = 0.70$, $Re_{out,is} = 120$ k with PIV (*a*), TRAF (*b*), and relative error (*c*)

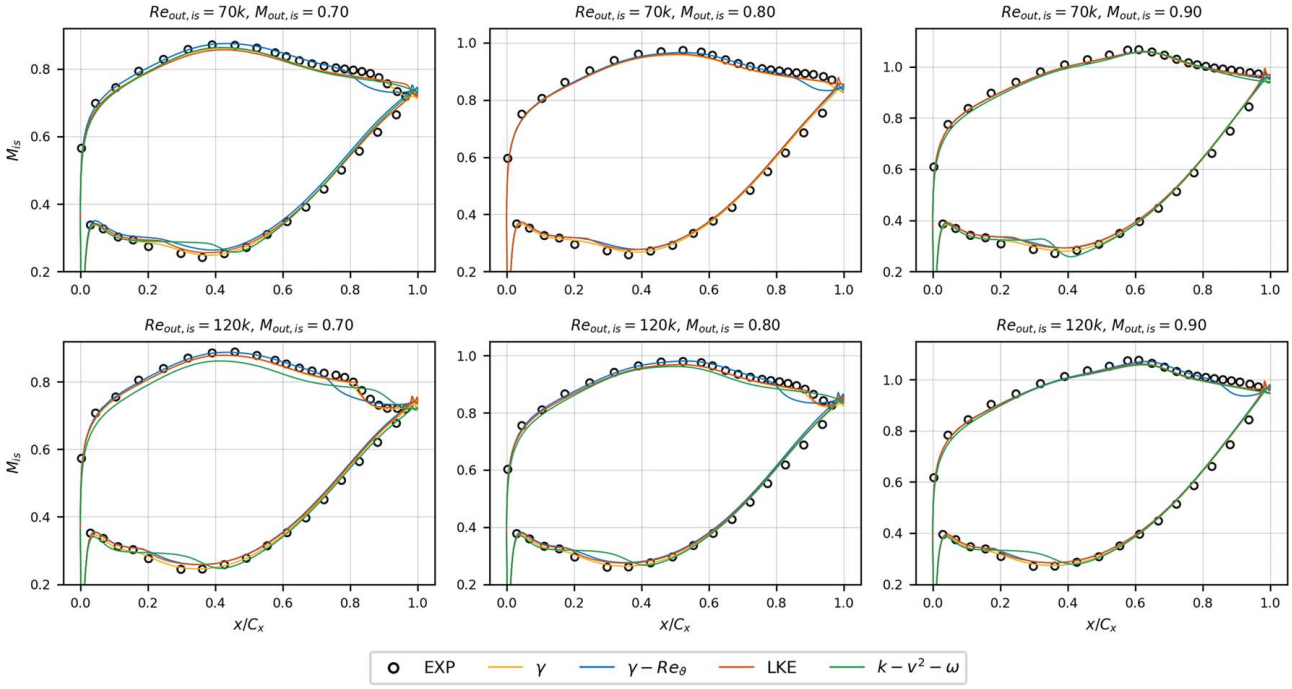

Fig. 11 Isentropic Mach number distribution on blade

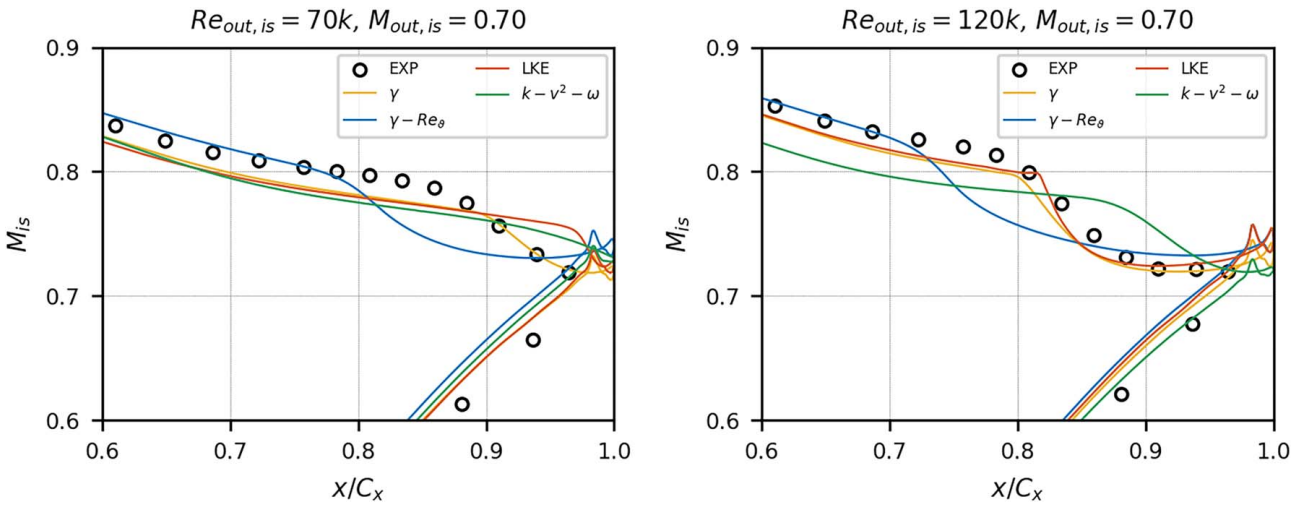

Fig. 12 Detail of the transition onset for $Ma_{out,is} = 0.70$

5.3 Wall Shear Stress Distributions. Wall shear stress profiles are shown in Fig. 13. To obtain accurate wall shear measurements with hot films, an extensive and extremely elaborate calibration of the sensors would be required. Such a calibration was not performed, and therefore, the experimental data only provide a qualitative measure of the wall shear distribution. Furthermore, the hot film measurements are not able to capture a reversed velocity with respect to the direction of flow. In Fig. 13, the uncalibrated hot film measurements are reported in Volt and, for the CFD comparison, the calculated wall shear stress was scaled in order to match the first measurement on the blade suction side.

On the pressure side, zero values of experimental quasi-wall shear stress can be observed, at $Re_{out,is} = 70k$, just downstream the blade leading edge up to 20% axial chord. They could indicate the presence of a separation bubble. At higher Reynolds numbers, quasi-wall shear stress values never touch the zero level, suggesting attached flow all over the blade pressure side. Indeed, all the calculations predict suction side boundary layer separation. For $Re_{out,is} = 70k$, reattachment points are located at about 25% axial chord, where measured values are already well above zero. The pressure side separation is predicted in a very similar way by the considered models and, probably, it is overestimated. The presence of a very small separation is predicted on the pressure side, even at higher Reynolds numbers, where measured quasi-wall shear stresses do not show any evidence of it. The different pressure side boundary layer behavior and related blockage effects are deemed to be responsible for the discussed discrepancies between computation and measurements in terms of M_{is} distributions.

On the suction side, on the other hand, it can be inferred that, at low Mach, the transition is actually induced by the separation bubble. Consistently, with what observed in terms of isentropic Mach number distributions, the γ and LKE models are the ones

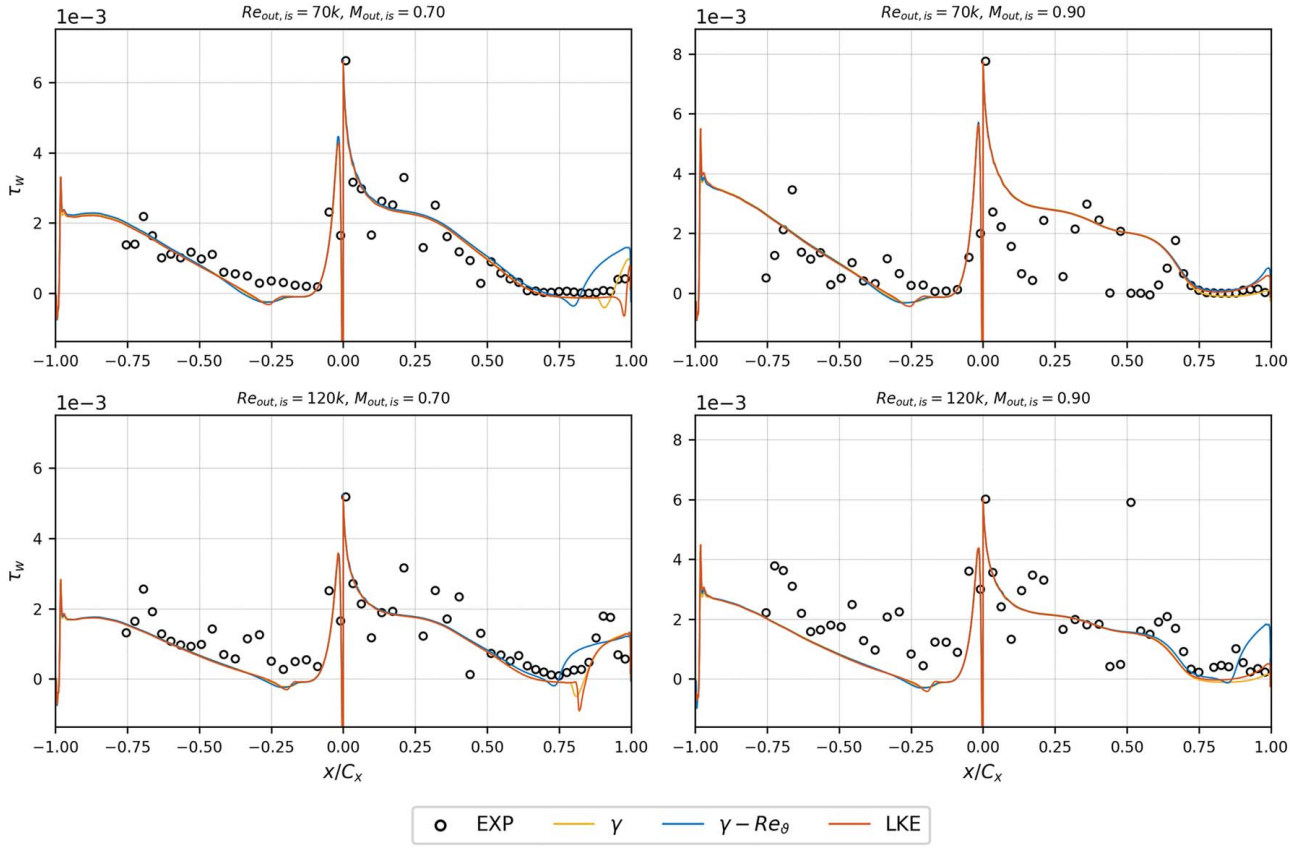

Fig. 13 Wall shear stress distribution on blade surface

that more closely resemble the transition path suggested by the quasi-wall shear stress distributions. At high Mach ($Ma_{out,is} = 0.90$), the effect of the shock wave impacting the suction side boundary layer can be inferred at approximately $x/C_x = 60\%$. However, the shock/boundary layer interaction does not seem to directly induce transition. All the calculations report that the transition starts downstream of the shock foot and close to the trailing edge. The behavior of the measured quasi-wall shear stress distributions is in line with these observations. The question regarding the transition mode, however, remains open. The LKE model seems to predict bypass transition in the attached boundary layer, while γ model (and $\gamma - \mathrm{Re}_{\theta,t}$ model at $\mathrm{Re}_{out,is} = 120k$) seems to calculate slightly negative shear stress downstream of the shock. Such predictions are consistent with the presence of a very shallow separation downstream of the shock that could play a role in the transition process. This could also be responsible for the triggering of early and abrupt transition by the $\gamma - \mathrm{Re}_{\theta,t}$ model at $\mathrm{Re}_{out,is} = 120k$.

To gain more insights in the transition path at high Mach number, a more detailed inspection of the numerical solutions has been conducted. For the LKE model prediction at $Ma_{out,is} = 0.9$ and $\mathrm{Re}_{out,is} = 120k$, Fig. 14 reports TKE isolines superimposed on stream-wise pressure gradient color contours. It can be appreciated how, downstream of the shock, the BL thickening accommodates a series of supersonic expansion (indicated with "E" in Fig. 14) and compression (indicated with "C" in Fig. 14) waves. In the vicinity of the wall, the first expansion wave virtually cancels the compression associated with the shock wave. This mechanism results in the smooth diffusion visible in the M_{is} distribution between the peak location and the trailing edge (Fig. 11). Due to the mild pressure gradient between the cascade throat and the trailing edge, transition is delayed downstream of shock location on the suction side and occurs freely and smoothly, in the bypass mode, at approximately $x/C_x = 85\%$.

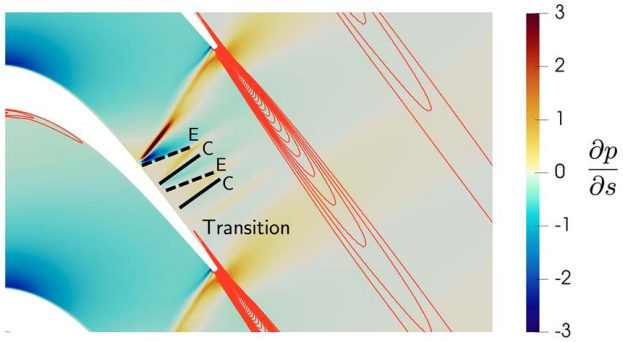

Fig. 14 Color contours of stream-wise pressure gradient and TKE isolines for $Ma_{out,is} = 0.9$, $Re_{out,is} = 120$ k

Experimental PIV visualizations are not sufficiently detailed for appreciating this flow mechanism that has nonetheless been detected in all the numerical simulations.

5.4 Outlet Plane. To characterize the total pressure loss in the wakes, measurements at Plane 06 are used, and in particular, the total pressure loss term $Y = 1 - p_{06}/p_{01}$ is examined as a function of the normalized tangential coordinate y/g. Figure 15 shows the total pressure loss profile at Plane 06 for the configurations already analyzed in terms of isentropic Mach and wall shear stress. The location $y/g = 0$ represents the position the wake peak would ideally have for an exit flow angle equal to the metal angle. Then, the plots in Fig. 15 also provide a qualitative measure of the flow deviation.

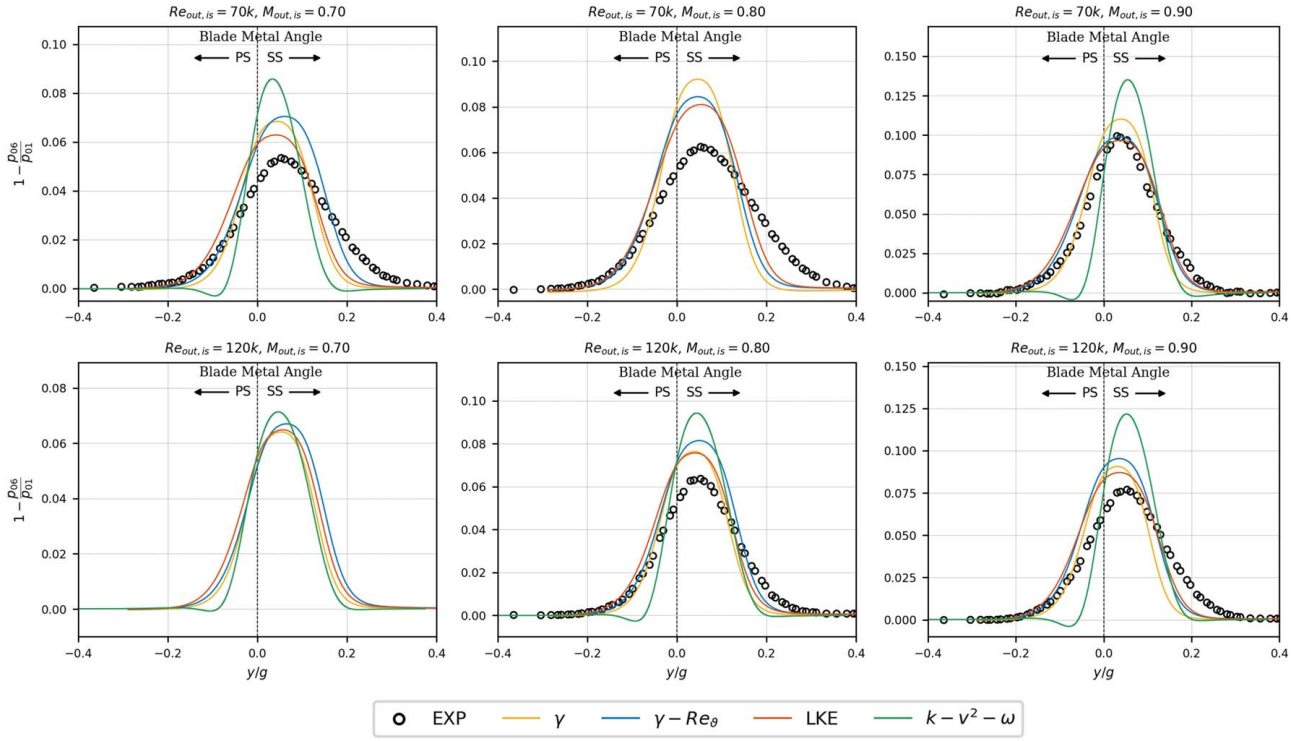

Fig. 15 Pitch-wise distribution of total pressure loss on Plane 06

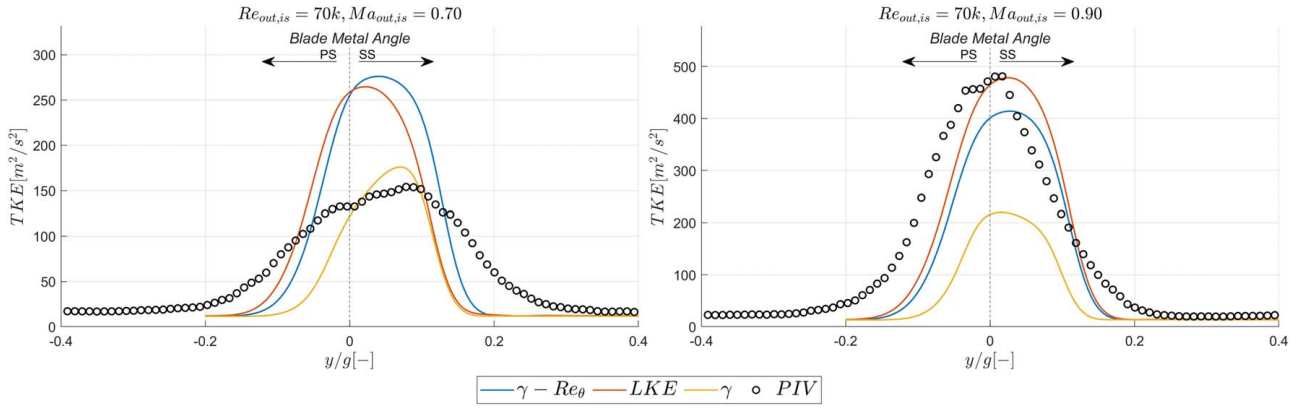

Fig. 16 Comparison of TKE profiles at Plane 06 between LKE, $\gamma - \mathrm{Re}_{\theta,t}$, γ and PIV

The agreement between computed and measured wake loss profiles is good at the nominal conditions ($\mathrm{Ma_{out,is}} = 0.9$, $\mathrm{Re_{out,is}} = 70\mathrm{k}$) except for the $k - v'^2 - \omega$ and tends to worsen as the exit Mach number decreases. Low Mach number flow configurations show the poorest agreement with measurements for all the considered models, both in terms of maximum loss peak and wake spreading. For $\mathrm{Ma_{out,is}} = 0.7 - 0.8$, the loss peak is larger and the wake width smaller relative to experimental data for all the calculations. The inability to correctly represent wake mixing is a quite well-known deficiency of RANS approaches, and several attempts have been made, by using data-driven explicit algebraic Reynolds stress models (EARSMs), to address this issue [21,42–45]). Low Mach number flow configurations are characterized by laminar separation of the suction side boundary layer and separated flow transition. Transitional separation bubbles result in a thick turbulent boundary layer after transition and reattachment, and this contributes to a more intense wake mixing. It can be seen that, while the γ model had better accuracy than LKE and $\gamma - \mathrm{Re}_{\theta,t}$ in terms of isentropic Mach, in the wakes, there is not that much difference. Interestingly, considering the $\mathrm{Ma_{out,is}} = 0.70$ and $\mathrm{Re_{out,is}} = 120\mathrm{k}$ case as an example, the LKE model was not able to capture the transition point as accurately as the γ model, but in terms of the wake, the latter seems to have a slightly worse distribution. The $k - v'^2 - \omega$ model does not lead to satisfactory results, consistently overestimating the wake loss peak while underestimating the wake width.

To gain more insights on the predicted wake mixing phenomenon and the consequent misrepresentation of wake loss profiles, pitch-wise distributions of TKE at Plane 06 are compared to those measured by PIV in Fig. 16. Only results by the best-performing models, namely the LKE, $\gamma - \mathrm{Re}_{\theta,t}$, and γ models are reported. First of all, two peaks in the TKE are observed in the experimental data, likely due to different turbulence breakdown dynamics between pressure and suction sides. However, CFD does not seem to capture this behavior, and its TKE profiles appear practically symmetrical. The only exception is provided by the

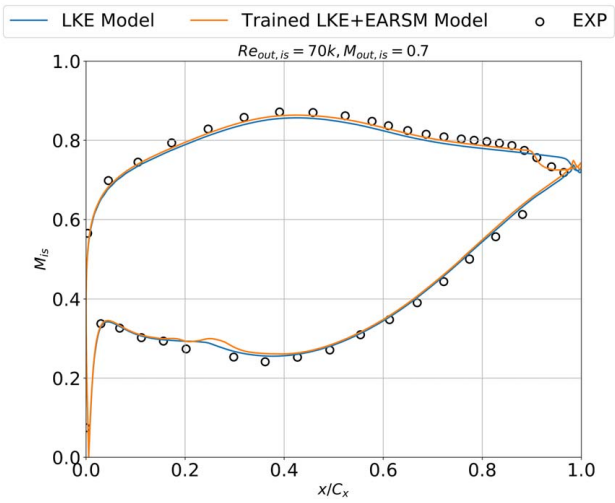

Fig. 17 Comparison of blade surface isentropic Mach number distributions between baseline LKE and trained LKE + EARSM models ($Re_{out,is} = 70$ k, $M_{out,is} = 0.7$)

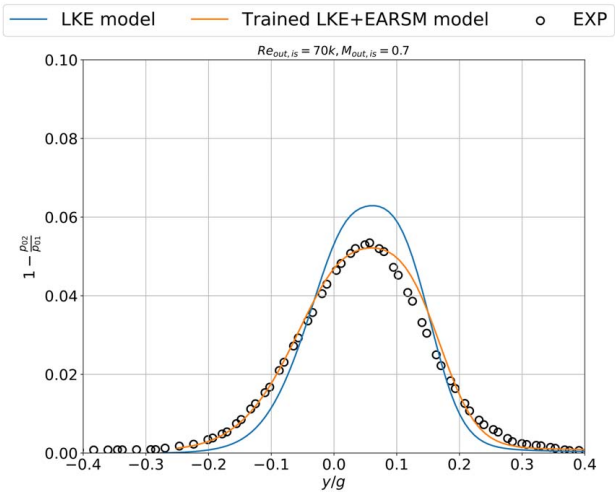

Fig. 18 Comparison of pitch-wise total pressure loss distributions on Plane 06 between baseline LKE and trained LKE + EARSM models ($Re_{out,is} = 70$ k, $M_{out,is} = 0.7$)

γ model, which, at low Mach numbers, has a slightly more inclined profile on the suction side thus better resembling the PIV data. In these conditions, the γ model seems also to provide the correct TKE level. However, the tangential spreading of the TKE profile appears severely underestimated. All the other models are substantially off and largely overestimate the TKE peak while maintaining a nonnegligible underestimation of the TKE in the peripheral region of the wake. Despite those differences, at low Mach numbers, the LKE model performs slightly better than the γ model in terms of wake loss profiles (Fig. 15). This suggests that a more realistic reproduction of the tangential extension of the TKE profile may be more important than capturing the overall TKE level. At the nominal conditions ($Ma_{out,is} = 0.9$, $Re_{out,is} = 70k$), the TKE profile obtained from the LKE model shows a satisfactory agreement with PIV measurements, and the $\gamma - Re_{\theta,t}$ model prediction is only slightly worse. Both models provide a very good reproduction of the wake loss profile (Fig. 15). In contrast, the γ model significantly underestimates both the peak and the tangential spreading of the experimental TKE profile, resulting in the worst agreement with measurements in terms of pitch-wise loss distribution.

Table 4 Mass-averaged loss coefficients at Plane 06 ($Re_{out,is} = 70k$, $M_{out,is} = 0.7$)

	EXP	LKE	Trained LKE + EARSM
$1 - \frac{p_{02}}{p_{01}}$	0.011	0.012	0.011

6 Preliminary Trained Model Results

In the previous section, it was mentioned how a data-driven training of transition and turbulence closures based on machine-learning approaches represents a promising strategy to improve both blade surface boundary layers and wake mixing predictions by traditional RANS approaches. In this section of the article, preliminary results obtained with a trained transition/turbulence model are presented to demonstrate the feasibility of such a strategy. The predictions obtained with a machine-learned closure for fully coupled transition and wake mixing predictions are presented in Figs. 17 and 18 in terms of the blade surface isentropic Mach number and pitch-wise wake total pressure loss distributions, respectively. Only the results for the case with $Re_{out,is} = 70k$ and $M_{out,is} = 0.7$ are reported for the sake of conciseness, but very similar outcomes have been obtained for all the other flow conditions. The LKE model was selected as the baseline transition closure, while an EARSM approach was adopted for improving wake mixing predictions. The employed machine-learning strategy is the one described in Refs. [43,46]. Transition and EARSM models were simultaneously trained using the SPLEEN cascade at four different flow conditions as training cases. The striking improvement achievable with the machine-learned model in the prediction of suction side separation bubble and pitch-wise wake loss distribution at Plane 06 can be clearly appreciated. Also, the prediction of integral mass-averaged loss coefficients at Plane 06 benefits from the improvements introduced by the data-driven model, as shown in Table 4.

7 Conclusion

A transonic LPT cascade for geared turbofan applications (SPLEEN C1 cascade) has been studied using RANS methods across a range of Reynolds and Mach numbers. Two different state-of-the-art CFD solvers have been employed, with a focus on various transition/turbulence models. Several modern transition-sensitive turbulence closures have been assessed against experimental data. They include classical intermittency-based approaches such as the $\gamma - Re_\theta$ and γ models, as well as less commonly used phenomenological closures in turbomachinery applications, such as the $k - v'^2 - \omega$ model and a newly formulated LKE-based framework. Two-dimensional calculations at mid-span have been carried out, and mesh-independent numerical results have been obtained through a careful grid dependency analysis. The selected grid size is considered to be compatible with design iteration requirements in terms of computational cost, even for 3D calculations.

A qualitative evaluation of the computed flow fields has been carried out by comparing Mach number and turbulence intensity contours with PIV experimental data. In terms of Mach number, such a comparison reports a satisfactory agreement between predictions and measurements. Specifically, at high Mach number, the supersonic region and the resulting passage shock in the throat region of the blade passage are well captured by the numerical calculations. However, relatively significant discrepancies are observed in the wake region. Despite the measured turbulence decay is accurately matched upstream the cascade leading edge, nonnegligible difference has been found between calculations and experiments in terms of freestream turbulence level within the blade passage.

Quasi-wall shear stress distributions reveal how the suction side boundary layer transition exhibits a multimodal path, shifting from the separated flow to the bypass mode as the exit isentropic

Mach number increases while almost independently from the Reynolds number. As a result, transition modeling has a crucial impact on the prediction of the blade surface isentropic Mach number distribution. Upon scrutinizing the adopted models, it can be concluded that the γ model yields the best performance, followed by the LKE framework. At high exit isentropic Mach numbers, when transition on the blade suction side occurs in the bypass mode, the best performing closures provide results that show satisfactory agreement with experiments on the entire range of Reynolds numbers. However, the spread between the predictions by the various models increases when lowering the Mach number, with the formation of a separation bubble on the blade suction side and the switch of transition to the separated flow mode. The major discrepancies among the various predictions and measurements are recorded for the lowest exit isentropic Mach number, and they are driven by differences in the computed transition onset and reattachment locations. Surprisingly, at high Mach numbers, where the passage shock interacts with the suction side boundary layer, transition is found to occur freely downstream of the shock foot. This observation is confirmed by blade surface quasi-wall shear stress distributions and it appears consistent with the particular compression-expansion waves train occurring on the uncovered part of the blade suction side, which is responsible for the establishment of a very smooth adverse pressure gradient.

Apart from the predictions from the $k - v'^2 - \omega$, which appears substantially off over the entire range of analyzed flow conditions, the agreement between calculations and experiments in terms of wake loss profiles is generally good at the cascade design point but progressively worsens when changing Mach and Reynolds numbers. Again, the worst predictions occur at the low Mach number cases. The discussed differences in how the various models reproduce the suction side separation bubble, which possibly lead to different boundary layer structures at the blade trailing edge, do not impact in a predictable manner on the calculated wake loss profiles. All models consistently overestimate the loss peak and underestimate the wake width. The mismatch in the pitch-wise distributions of wake losses is more likely due to the known limitation of linear eddy viscosity closures to realistically model the wake mixing. This observation is reinforced by the comparison between calculations and measurements in terms of TKE profiles at Plane 06. At design conditions, the good agreement between the experimental pitch-wise TKE profile and the LKE and $\gamma - \mathrm{Re}_{\theta,t}$ predictions result in an almost perfect reproduction of the wake loss profiles. However, at low Mach number, the measured TKE field in Plane 06 is radically mismatched by the numerical results, which clearly indicate a severe underestimation of the wake mixing process. The separation bubbles that characterize the flow topologies at low Mach numbers result in a thick turbulent boundary layer after transition and reattachment, leading to a more intense wake mixing, which is not captured by the considered models. Machine-learned transition/turbulence closures have proven to be effective in addressing the inaccuracies of the considered RANS approaches. The data-driven training of fully coupled transition and nonlinear EARSMs is therefore highly desirable to achieve realistic predictions when exploring off-design conditions for transonic LPT blades during design phases.

Acknowledgment

The authors of the University of Florence acknowledge the contribution of the ICSC Italian Research Center on High Performance Computing, Big Data, and Quantum Computing, funded by the European Union NextGenerationEU (CUP B83C22002830001).

Conflict of Interest

There are no conflicts of interest.

Data Availability Statement

The data and information that support the findings of this article are freely available at: https://zenodo.org/records/13712768

Nomenclature

a = Speed of sound (m/s)
k = Turbulent kinetic energy (m^2/s^2)
p = Pressure (Pa)
C = Cascade true chord (m)
T = Temperature (K)
V = Velocity magnitude (m/s)
C_{ax} = Cascade axial chord (m)
L_t = Turbulent length scale (m)

Greek Symbols

β = Flow angle (deg)
μ = Dynamic viscosity (kg/m/s)
ω = Specific dissipation rate (1/s)

Superscripts and Subscripts

in = Inlet plane
out = Outlet plane
is = Isentropic
iso = Isotropic

Dimensionless Groups

Ma = Mach number, V/a
Re = Reynolds number, $\rho LV/\mu$
Tu = Turbulence intensity, u'/V

Acronyms

B2B = Blade to blade
CFD = Computational fluid dynamics
LKE = Laminar kinetic energy
LPT = Low-pressure turbine
PIV = Particle image velocimetry
(U)RANS = (Unsteady)Reynolds-averaged Navier–Stokes
SPLEEN = Secondary and Leakage Flow Effects in High-Speed Low-Pressure Turbines
TKE = Turbulent kinetic energy
XW = Cross-wire probe

References

[1] Kurzke, J., 2009, "Fundamental Differences Between Conventional and Geared Turbofans," Proceedings of the ASME Turbo Expo, Orlando, FL, June 8–12, pp. 145–153.
[2] Hodson, H. P., and Howell, R. J., 2005, "Bladerow Interactions, Transition, and High-Lift Aerofoils in Low-Pressure Turbines," Annu. Rev. Fluid Mech., **37**(1), pp. 71–98.
[3] Malzacher, F. J., Gier, J., and Lippl, F., 2006, "Aerodesign and Testing of an Aeromechanically Highly Loaded LP Turbine," ASME J. Turbomach., **128**(4), pp. 643–649.
[4] Mayle, R. E., 1991, "The 1991 IGTI Scholar Lecture: The Role of Laminar-Turbulent Transition in Gas Turbine Engines," ASME J. Turbomach., **113**(4), pp. 509–536.
[5] Durbin, P. A., 2017, "Perspectives on the Phenomenology and Modeling of Boundary Layer Transition," Flow Turbul. Combust., **99**(1), pp. 1–23.
[6] Sandberg, R. D., Michelassi, V., Pichler, R., Chen, L., and Johnstone, R., 2015, "Compressible Direct Numerical Simulation of Low-Pressure Turbines—Part I: Methodology," ASME J. Turbomach., **137**(5), p. 051011.
[7] Michelassi, V., Chen, L.-W., Pichler, R., and Sandberg, R. D., 2015, "Compressible Direct Numerical Simulation of Low-Pressure Turbines—Part II: Effect of Inflow Disturbances," ASME J. Turbomach., **137**(7), p. 071005.
[8] Michelassi, V., Chen, L., Pichler, R., Sandberg, R., and Bhaskaran, R., 2016, "High-Fidelity Simulations of Low-Pressure Turbines: Effect of Flow Coefficient and Reduced Frequency on Losses," ASME J. Turbomach., **138**(11), p. 111006.
[9] Sandberg, R. D., and Michelassi, V., 2019, "The Current State of High-Fidelity Simulations for Main Gas Path Turbomachinery Components and Their Industrial Impact. Flow," Turbul. Combust., **102**(4), pp. 797–848.

[10] Dick, E., and Kubacki, S., 2017, "Transition Models for Turbomachinery Boundary Layer Flows: A Review," Int. J. Turbomach. Propuls. Power, **2**(2), p. 4.
[11] Langtry, R. B., and Menter, F. R., 2009, "Correlation-Based Transition Modeling for Unstructured Parallelized Computational Fluid Dynamics Codes," AIAA J., **47**(12), pp. 2894–2906.
[12] Ge, X., Arolla, S., and Durbin, P., 2014, "A Bypass Transition Model Based on the Intermittency Function," Flow, Turbul. Combust., **93**, pp. 37–61.
[13] Kubacki, S., Simoni, D., Lengani, D., and Dick, E., 2020, "An Extended Version of an Algebraic Intermittency Model for Prediction of Separation-Induced Transition at Elevated Free-Stream Turbulence Level," Int. J. Turbomach. Propuls. Power, **5**(4), p. 28.
[14] Menter, F. R., Smirnov, P. E., Liu, T., and Avancha, R., 2015, "A One-Equation Local Correlation-Based Transition Model," Flow, Turbul. Combust., **95**, pp. 583–619.
[15] Mayle, R. E., and Schulz, A., 1997, "The Path to Predicting Bypass Transition," ASME J. Turbomach., **119**(3), pp. 405–411.
[16] Walters, D. K., and Cokljat, D., 2008, "A Three-Equation Eddy-Viscosity Model for Reynolds-Averaged Navier–Stokes Simulations of Transitional Flow," ASME J. Fluids Eng., **130**(12), p. 121401.
[17] Pacciani, R., Marconcini, M., Fadai-Ghotbi, A., Lardeau, S., and Leschziner, M. A., 2011, "Calculation of High-Lift Cascades in Low Pressure Turbine Conditions Using a Three-Equation Model," ASME J. Turbomach., **133**(3), p. 031016.
[18] Pacciani, R., Marconcini, M., Arnone, A., and Bertini, F., 2011, "An Assessment of the Laminar Kinetic Energy Concept for the Prediction of High-Lift, Low-Reynolds Number Cascade Flows," Proc. Inst. Mech. Eng. Part A J. Power Energy, **225**(7), pp. 995–1003.
[19] Pacciani, R., Fang, Y., Metti, L., Marconcini, M., and Sandberg, R., 2025, "A Reformulation of the Laminar Kinetic Energy Model to Enable Multi-Mode Transition Predictions," Flow Turbul. Combust., **114**(1), pp. 81–116.
[20] Lopez, M., and Walters, D. K., 2016, "Prediction of Transitional and Fully Turbulent Flow Using an Alternative to the Laminar Kinetic Energy Approach," J. Turbul., **17**(3), pp. 253–273.
[21] Akolekar, H. D., Weatheritt, J., Hutchins, N., Sandberg, R. D., Laskowski, G., and Michelassi, V., 2019, "Development and Use of Machine-Learnt Algebraic Reynolds Stress Models for Enhanced Prediction of Wake Mixing in Low-Pressure Turbines," ASME J. Turbomach., **141**(4), p. 041010.
[22] Rosafio, N., Lopes, G., Salvadori, S., Lavagnoli, S., and Misul, D. A., 2023, "RANS Prediction of Losses and Transition Onset in a High-Speed Low-Pressure Turbine Cascade," Energies, **16**(21), p. 7348.
[23] Simonassi, L., Lopes, G., Gendebien, S., Torre, A. F. M., Patinios, M., Lavagnoli, S., Zeller, N., and Pintat, L., 2022, "An Experimental Test Case for Transonic Low-Pressure Turbines–Part I: Rig Design, Instrumentation and Experimental Methodology," Turbo Expo: Power for Land, Sea, and Air, Rotterdam, Netherlands, June 13–17, Vol. 10B, p. V10BT30A012.
[24] Lopes, G., Simonassi, L., Torre, A., Patinios, M., and Lavagnoli, S., 2022, "An Experimental Test Case for Transonic Low-Pressure Turbines-Part 2: Cascade Aerodynamics at On- and Off-Design Reynolds and Mach Numbers," Turbo Expo: Power for Land, Sea, and Air, Rotterdam, Netherlands, June 13–17, Vol. 10B, p. V10BT30A027.
[25] Okada, M., Simonassi, L., Lopes, G., and Lavagnoli, S., 2024, "Particle Image Velocimetry Measurements in a High-Speed Low-Reynolds Low-Pressure Turbine Cascade," ASME J. Turbomach., **146**(3), p. 031010.
[26] Tene Hedje, P., Bricteux, L., Bechane, Y., and Lavagnoli, S., 2024, "Large Eddy Simulations of a High-Speed Low-Pressure Turbine Cascade At Subsonic and Transonic Mach Numbers," Turbo Expo: Power for Land, Sea, and Air, London, UK, June 24–28, Vol. 12C, p. V12CT32A032.
[27] Perkins, D. W., and Duchaine, F., 2024, "Large-Eddy Simulations of a High-Speed Low-Pressure Turbine Cascade With Purge Flow," Turbo Expo: Power for Land, Sea, and Air, London, UK, June 24–28, Vol. 12C, p. V12CT32A011.
[28] Hullin, L., Gonzalez-Martino, I., and Bonnal, B., 2024, "Unsteady Flow Simulations of a Transonic Low-Pressure Turbine Cascade," Turbo Expo: Power for Land, Sea, and Air, London, UK, June 24–28, Vol. 12B, p. V12BT30A013.
[29] Adami, P., Salvadori, S., and Chana, K. S., 2006, "Unsteady Heat Transfer Topics in Gas Turbine Stages Simulations," Turbo Expo: Power for Land, Sea, and Air, Barcelona, Spain, May 8–11, Vol. 6, pp. 1733–1744.
[30] Adami, P., Belardini, E., Martelli, F., and Michelassi, V., 2001, "Unsteady Rotor/Stator Interaction: An Improved Unstructured Approach," Turbo Expo: Power for Land, Sea, and Air, New Orleans, LA, June 4–7, Vol. 1, p. V001T03A051.
[31] Adami, P., Martelli, F., and Michelassi, V., 2000, "Three-Dimensional Investigations for Axial Turbines by an Implicit Unstructured Multi-Block Flow Solver," Turbo Expo: Power for Land, Sea, and Air, Munich, Germany, May 8–11, Vol. 1, p. V001T03A108.
[32] Rosafio, N., Salvadori, S., and Misul, D. A., 2024, "Implementation of a High-Order Spatial Discretization Into a Finite Volume Solver: Applications to Turbomachinery Test Cases Using an Eddy-Viscosity Turbulence Closure," Heliyon, **10**(16), p.e36478.
[33] Roe, P. L., 1981, "Approximate Riemann Solvers, Parameter Vectors, and Difference Schemes," J. Comput. Phys., **43**(2), pp. 357–372.
[34] Jalali, A., and Ollivier Gooch, C., 2012, "Accuracy Assessment of Finite Volume Discretizations of Diffusive Fluxes on Unstructured Meshes," 50th AIAA Aerospace Sciences Meeting Including the New Horizons Forum and Aerospace Exposition, Nashville, TN, Jan. 9–12, p. 608.
[35] Ollivier Gooch, C., 1997, "High-Order ENO Schemes for Unstructured Meshes Based on Least-Squares Reconstruction," 35th Aerospace Sciences Meeting and Exhibit, Reno, NV, Jan. 6–9, p. 540.
[36] Saad, Y., and Schultz, M. H., 1986, "GMRES: A Generalized Minimal Residual Algorithm for Solving Nonsymmetric Linear Systems," SIAM J. Sci. Comput., **7**(3), pp. 856–869.
[37] Xu, S., Mohanamuraly, P., Wang, D., and Müller, J.-D., 2020, "Newton–Krylov Solver for Robust Turbomachinery Aerodynamic Analysis," AIAA J., **58**(3), pp. 1320–1336.
[38] Arnone, A., and Pacciani, R., 1997, "Numerical Prediction of Trailing Edge Wake Shedding," Proceedings of the ASME 1997 International Gas Turbine and Aeroengine Congress and Exhibition, Orlando, FL, June 2–5, ASME, p. V001T03A020. .
[39] Pacciani, R., Marconcini, M., and Arnone, A., 2019, "Comparison of the AUSM$^+$-Up and Other Advection Schemes for Turbomachinery Applications," Shock Waves, **29**(5), pp. 705–716.
[40] Pacciani, R., Marconcini, M., Bertini, F., Rosa Taddei, S., Spano, E., Zhao, Y., Akolekar, H. D., Sandberg, R. D., and Arnone, A., 2021, "Assessment of Machine-Learned Turbulence Models Trained for Improved Wake-Mixing in Low-Pressure Turbine Flows," Energies, **14**(24), p. 8327.
[41] Stimpson, C. J., Ernst, C. D., Knupp, P., Pebay, P. P., and Thompson, D., 2007, "The Verdict Library Reference Manual," https://public.kitware.com/Wiki/images/6/6b/VerdictManual-revA.pdf.
[42] Akolekar, H. D., Zhao, Y., Sandberg, R. D., and Pacciani, R., 2021, "Integration of Machine Learning and Computational Fluid Dynamics to Develop Turbulence Models for Improved Low-Pressure Turbine Wake Mixing Prediction," ASME J. Turbomach., **143**(12), p. 121001.
[43] Akolekar, H. D., Pacciani, R., Waschkowski, F., and Zhao, Y., 2022, "Multi-Objective Development of Machine-Learnt Closures for Fully Integrated Transition and Wake Mixing Predictions in Low Pressure Turbines," Turbo Expo: Power for Land, Sea, and Air, Rotterdam, Netherlands, June 13–17, Vol. 10C, p. V10CT32A013.
[44] Frey Marioni, Y., Cassinelli, A., Adami, P., Sherwin, S., Vazquez Diaz, R., and Montomoli, F., 2022, "Development of Machine-Learnt Turbulence Closures for Wake Mixing Predictions in Low-Pressure Turbines," Turbo Expo: Power for Land, Sea, and Air, Rotterdam, Netherlands, June 13–17, Vol. 10C, p. V10CT32A032.
[45] Pacciani, R., Marconcini, M., Arnone, A., Bertini, F., Spano, E., Rosa Taddei, S., and Sandberg, R. D., 2024, "Improvements in the Prediction of Steady and Unsteady Transition and Mixing in Low-Pressure Turbines by Means of Machine-Learnt Closures," ASME J. Turbomach., **146**(5), p. 051009.
[46] Fang, Y., Zhao, Y., Akolekar, H. D., Ooi, A. S., Sandberg, R. D., Pacciani, R., and Marconcini, M., 2024, "A Data-Driven Approach for Generalizing the Laminar Kinetic Energy Model for Separation and Bypass Transition in Low- and High-Pressure Turbines," ASME J. Turbomach., **146**(9), p. 091005.